HM Hochschule für angewandte Wissenschaften München
Alexander Edelemann, supervised by Prof. Schindler

Praktikum Nanotechnik
December 29, 2024

Porous Silicon – Pre-Assignment-Report

CONTENTS

1 Dielectric Mirror 1

2 Quantum wires, band structure and luminescence wavelength 2

3 Ellipsometry Theory 3

1 DIELECTRIC MIRROR

Multi-layer optical thin-film coatings consist of a series of dielectric material layers designed to control the reflectivity of light they are exposed to. The effectiveness of these coatings is rooted in the principles of optical interference, wherein reflectivity depends on the constructive and destructive interference of light at the interfaces of each layer within the stack [1]. Dielectric mirrors, also known as Bragg mirrors or interference mirrors, aim to maximize reflectivity for a particular wavelength range. They are constructed from alternating layers of materials with differing refractive indices, typically deposited at nanometer-scale thicknesses. In its simplest form the thickness of each layer is designed to be a quarter of the particular wavelength they intend to reflect. However, these multi-layer coatings can be engineered to exhibit broad spectral characteristics, allowing them to function effectively across a range of wavelengths. These mirrors are fundamental for laser cavities where mirror bandwidth becomes significant for the generation of ultrashort pulses [2]. Moreover, dielectric multi-layer stacks are used for thin-film beamsplitters, which can be found in countless optical applications [3]. Additional applications extend to hot mirrors, which reflect near-infrared (NIR) and infrared (IR) wavelengths while permitting the passage of ultraviolet (UV) and visible light. In contrast, cold mirrors reflect UV and visible light, allowing NIR and IR to transmit through. Hot mirrors are frequently utilized in projection systems, where they effectively redirect and manage the heat generated by high-intensity lamps, thereby safeguarding components and preventing system overheating. Meanwhile, cold mirrors are increasingly valued in automotive applications, particularly in heads-up displays (HUDs) [4]. For anti-reflective applications, these multi-layer stacks are engineered to minimize the reflection from surfaces, thereby increasing the transmission of light through the substrate. The principle is the same as for reflective coatings, relying on interference effects between multiple layers. Anti-reflective coatings are widely used in lenses for cameras and glasses, displays, solar panels, and other optical devices where reducing glare and maximizing light transmission is crucial [5].

Basic Theory The fundamental theory of multi-layer optical thin-film coatings is discussed here, focusing on the simplest case of two different dielectric materials with refractive indices $\hat{n}_1$ and $\hat{n}_2$. These refractive indices are generally complex to account for material absorption; however, for this discussion, their exact value is not of importance. Additionally, we assume $n_1 > n_2$, which could represent materials such as SiO2 ($n = 1.46$) and TiO2 ($n = 2.3$). As mentioned, the thickness of each layer is set to one-quarter of the wavelength of the incident light to create a highly reflective mirror. We will also examine the case where the layer thickness equals half the wavelength. Furthermore, we will analyze how the order of the two layers affects their performance for specific applications. These four scenarios are illustrated in Fig. 1. As shown, the incident wave is reflected at every interface between layers, and the resulting reflected waves interfere with one another. Importantly, for the reflected wave, a π-phase shift occurs at each interface where the wave transitions to a material with a higher refractive index. Hence, a π-phase shift occurs at the surface of the stack regardless of which layer it constitutes. Within the stack they occur at transitions n_2 to n_1. It is also important to note that the transitioning wave is not affected by a phase shift. The relative phase positions of the individual reflected beams ultimately determine the intensity of the total reflected light. From the figure we can see that a layer thickness of half the wavelength results in the exact adverse effect, generating pairs of beams that interfere destructively with on another. By comparing Fig. 1a and Fig. 1b it can be observed that both constructive and destructive interference are strongest when the topmost layer has the higher refractive index (in our case n_1). This is, because the amplitude decays with the distance traveled by the wave. In other words, the size of the amplitude decreases with the number of stacks the reflected wave has traveled through. It is therefore important that the interference of the waves with the biggest amplitudes result in the interference pattern intended for the application. From Fig. 1b it can be observed that the two first reflections interfere destructively, whereas the rest of the waves interfere constructively and vice versa. Finally, it should be noted that increasing the number of layers in the stack amplifies either the reflectivity or anti-reflectivity of the system, depending on the design.

Fabrication The optical performance of multilayer thin films relies heavily on maintaining uniformity throughout the structure. Achieving this requires precise control of layer thickness to en-

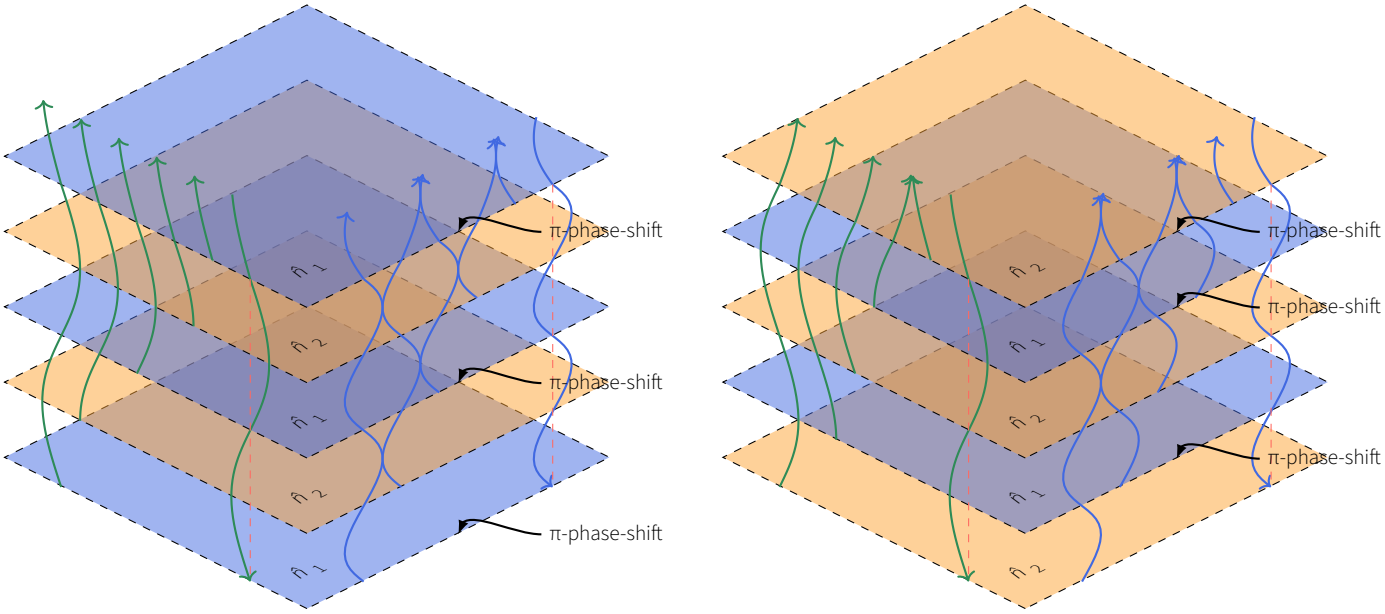

(a) Topmost layer comprises material with refractive index n_1.

(b) Topmost layer comprises material with refractive index n_2.

Fig. 1 | **Illustration of the operating principle of a dielectric mirror.** The refractive indices are defined such that $n_1 > n_2$.

sure accurate interference patterns and material consistency to minimize scattering and absorption. A smooth surface is also critical, as it reduces light scattering and enhances optical clarity. Additionally, strong interlayer adhesion is vital for preventing delamination and reducing the risk of defects. The deposition method, along with careful regulation of environmental factors, is equally important in achieving uniform coverage and preserving the desired properties of each layer [5]. Several methods are commonly employed in the fabrication of thin film multilayers, each offering unique advantages. Physical Vapor Deposition (PVD) methods, such as evaporation and sputtering are widely used, chemical vapor deposition (CVD), atomic layer deposition (ALD) and Sol-Gel coating are common alternatives. Evaporation involves vaporizing the material and condensing it onto a substrate for high-purity layers with excellent thickness control, although it often requires high-vacuum conditions. Sputtering, on the other hand, provides good control over layer thickness and uniformity and is versatile for a wide range of materials, making it suitable for complex multilayer structures. CVD offers highly conformal coatings over large areas, ideal for industrial applications requiring uniformity and high material purity. ALD provides atomic-scale precision in layer thickness, perfect for applications demanding ultra-thin layers and excellent uniformity, though it is a slower process. Sol-Gel Coating, involving liquid solution precursors, is cost-effective for large-area coatings but lacks the precision of vacuum-based techniques. Tab. 1 should give a broad overview of how these methods compare [6, 3, 7, 8, 9].

Fabricating dielectric mirrors using porous silicon (pSi) is less common than employing traditional dielectric materials such as SiO2 (silicon dioxide) and TiO2 (titanium dioxide). However, pSi offers a unique advantage: its refractive index can be precisely tuned by controlling its porosity. Since porosity is a linear function of the current density for a given HF concentration and anodization time, a periodic pulsing technique alternating between two different current densities has become an effective method for fabricating multi-layer pSi films. One of the significant advantages of pSi for dielectric mirrors is its compatibility with silicon-based technologies, making it highly attractive for integrated optics and on-chip photonic applications. Additionally, its high porosity results in low refractive indices that are difficult to achieve with conventional materials, enabling a wider range of refractive index contrast. This property allows for the fabrication of dielectric mirrors with exceptional reflectivity and enhanced tunability for specific wavelength ranges. Despite these benefits, the widespread adoption of pSi in dielectric mirrors is limited by challenges in controlling porosity with high precision and ensuring mechanical stability. The fragile nature of pSi structures compared to more robust dielectric materials adds complexity to the fabrication process, making it less appealing for large-scale production [10, 11].

Fabrication Method	Precision	Uniformity	Material Flexibility	Cost & Speed
Evaporation (PVD)	High	Moderate	Moderate	Moderate
Sputtering (PVD)	High	Good	High	Moderate
Chemical Vapor Deposition (CVD)	Moderate	Excellent	High	High
Atomic Layer Deposition (ALD)	Excellent	Excellent	High	Slow
Sol-Gel Coating	Moderate	Moderate	Moderate	Cost-effective, fast

Tab. 1 | **Comparison of dielectric mirror fabrication methods.**

2 QUANTUM WIRES, BAND STRUCTURE AND LUMINESCENCE WAVELENGTH

Shrinking structures to a point where the Boltzmann model (diffusive charge transport) is no longer applicable because the wave nature of the electrons has to be taken into account are described by the so called mesoscopic transport model (ballistic transport). Such is the case for quantum wires – semiconductor nanostructures that confine the motion of electrons or holes in two spatial

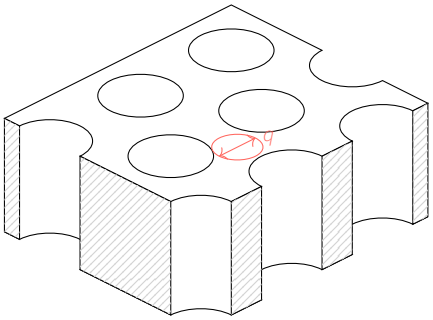

Fig. 2 | **Schematic illustration of the surface of porous silicon.** The circular cross section of a quantum wire of diameter q is indicated in red.

dimensions, allowing them free movement only along the remaining dimension. The quantum confinement in wires leads to discrete energy levels, similar to those observed in quantum dots, but with distinct characteristics due to their elongated, line-like shape. This confinement alters the electronic and optical properties of the material significantly, producing phenomena that are not present in bulk materials [12, 13].

Porous silicon consisting of a network of very small pores and walls created by electrochemical etching of crystalline silicon can exhibit properties of quantum wires. Understanding this phenomenon requires insight into the underlying dissolution chemistry of silicon in hydrofluoric acid. The theory is well documented in [14, 15, 16, 17] and shall not be discussed in detail here. Under low pH conditions, corresponding to low hydroxide concentrations, silicon surfaces are generally resistant to hydrofluoric acid attack. If the silicon is under anodic bias, the formation of porous layers is observed as long as the reaction is limited by the charge-supply of the electrode and not by ionic diffusion in the electrolyte. This condition is fulfilled for current densities below a HF concentration dependent, critical current density j_c. At such conditions, holes reaching the surface – from the bulk as majority carriers in the case of p-Si, by electron-hole pair generation by e.g. backside illumination in the case of n-Si – polarize the established Si-H bonds (hydrogen passivation) thereby allowing attacks on these bonds by fluoride ions. It is important to understand that the silicon-electrolyte interface's band structure resembles that of a Schottky barrier, forming a space charge region whose width varies with the silicon's doping concentration. This doping concentration dictates the dissolution reaction's stopping point, as the walls between pores reach a certain thickness. For lower doping concentrations, this will happen due to charge carrier depletion at the Si-electrolyte interface resulting from the walls reaching the size of the depletion region. In contrast, higher doping concentrations in p-type silicon demonstrate that dissolution ceases before the walls are sufficiently thin to induce depletion, suggesting that quantum confinement of charge carriers emerges due to the very small dimensions of the walls. This region, resembling a quantum wire, is depicted in Fig 2. As demonstrated in the work of Lehmann and Gösele [15], the ground state (kinetic) energy of a charge carrier confined within this quantum wire can be approximated using

$$\Delta E = \frac{h^2}{4m^* q^2},$$

assuming a square cross section of the side length q. This approximation is in reasonable agreement with experimental data regarding the increase in bandgap energy E_g, which ranges from a few hundred milli-electron volts to several electron volts. Consequently, the luminescence wavelength,

$$\lambda = \frac{hc}{E_g}$$

can extend into the visible spectrum. This suggests the potential for silicon-based optoelectronic devices, leveraging visible light emission. However, photon generation through electron-hole recombination competes with non-radiative recombination processes, which diminishes efficiency. The quantum efficiency is defined as the ratio of the radiative recombination rate (W_R) to the total recombination rate, which is the sum of W_R and the non-radiative recombination rate (W_{NR}):

$$\text{Quantum Efficiency} = \frac{W_R}{W_R + W_{NR}}.$$

Experimental results indicate that improving quantum efficiency has so far been achieved primarily by reducing W_{NR}. While this reduces non-radiative losses, it also slows the luminescence decay, leading to longer carrier lifetimes. This presents a significant challenge for the use of porous silicon in fast-switching optoelectronic devices, where rapid response times are essential [17].

3 ELLIPSOMETRY THEORY

To understand the operating principle of ellipsometry, it is essential to first examine light propagation at interfaces between media with differing refractive indices. For this purpose, we will provide an overview of the relevant governing equations. While their derivation is not particularly complex, it is rather lengthy and is extensively covered in standard references such as [1]. Thus, the detailed derivation will not be included in this discussion. The variables used in the following explanation are depicted in Figure 3.

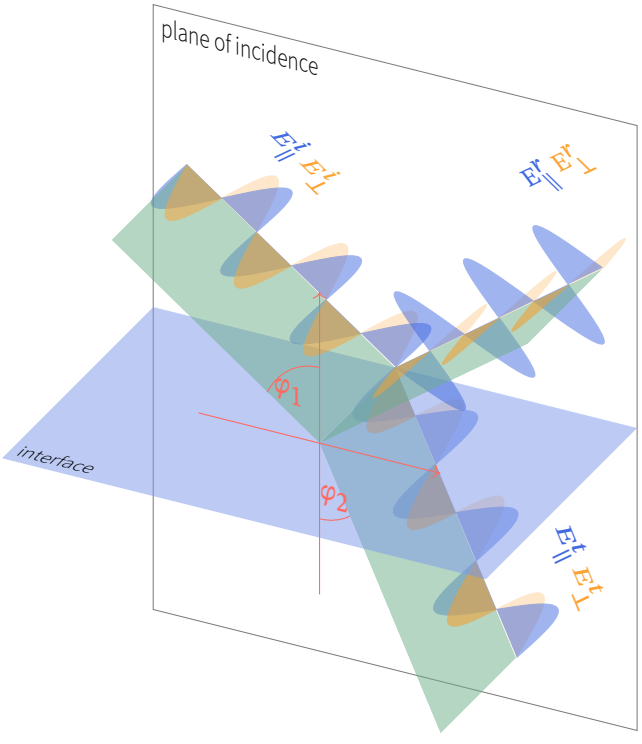

Fig. 3 | Plane wave propagation at interface.

It is well established that the angle of the incident wave equals the angle of the reflected wave. For the transmitted wave, however, the relationship between the angle of incidence (φ_1) and the angle of refraction (φ_2) is described by Snell's law:

$$\frac{\sin(\varphi_1)}{\sin(\varphi_2)} = \frac{n_2}{n_1} \tag{1}$$

where n_1 and n_2 are the refractive indices of the respective media.

To describe the change in the amplitudes of the incident and reflected waves, it is necessary to consider the polarization of the wave. The electric field vector (E-vector) of an electromagnetic wave can always be split into components that are perpendicular and parallel to the plane of incidence (refer to Fig. 3). In this figure, there is no phase difference between these components, indicating that the light is linearly polarized. Introducing a phase shift between the components leads to elliptically polarized light, and specifically, a phase difference of $\pi/2$ results in circular polarization. This means that the trajectory of the E-vector, when viewed along the propagation axis, traces an ellipse or a circle. By applying the continuity conditions for the electric (E) and magnetic (B) fields at the interface – derived from Maxwell's equations – we arrive at the Fresnel equations, also known as Fresnel coefficients. These equations provide a mathematical framework for determining the amplitude and phase of the different polarization components of reflected and transmitted waves. As for polarization perpendicular to the plane of incidence, the following relationship between the amplitudes of reflected and incident wave, denoted as r_s, exists:

$$\frac{E^r_\perp}{E^i_\perp} = \frac{\sin(\varphi_1 - \varphi_2)}{\sin(\varphi_1 + \varphi_2)} = r_s \tag{2}$$

For the relationship between the perpendicular amplitudes of the transmitted and the incident wave, denoted as t_s, we obtain:

$$\frac{E^t_\perp}{E^i_\perp} = \frac{2\sin(\varphi_2)\cos(\varphi_1)}{\sin(\varphi_1 + \varphi_2)} = t_s \tag{3}$$

For the value denoted as r_p for the parallel components we arrive at

$$\frac{E^r_\parallel}{E^i_\parallel} = \frac{\tan(\varphi_1 - \varphi_2)}{\tan(\varphi_1 + \varphi_2)} = r_p \tag{4}$$

and for t_p we obtain:

$$\frac{E^t_\perp}{E^i_\perp} = \frac{2\sin(\varphi_2)\cos(\varphi_1)}{\sin(\varphi_1 + \varphi_2)\cos(\varphi_1 - \varphi_2)} = t_p \tag{5}$$

The above equations can be expressed using the refractive indices by inserting Snell's law (1). When n_1 and n_2 are complex, the Fresnel equations still hold.

A commonly employed setup for an ellipsometry experiment is illustrated schematically in Fig. 4. This setup comprises several key components: a light source, which typically employs monochromatic or coherent sources such as lasers; a polarizer; two compensators; an analyzer; and a detector. These components function collectively as follows: The unpolarized light emitted by the source first passes through the polarizer, which converts it to linearly polarized light. This light comprises two components: one parallel to the plane of incidence, known as p-polarized light, and one perpendicular to it, called s-polarized light. The compensator

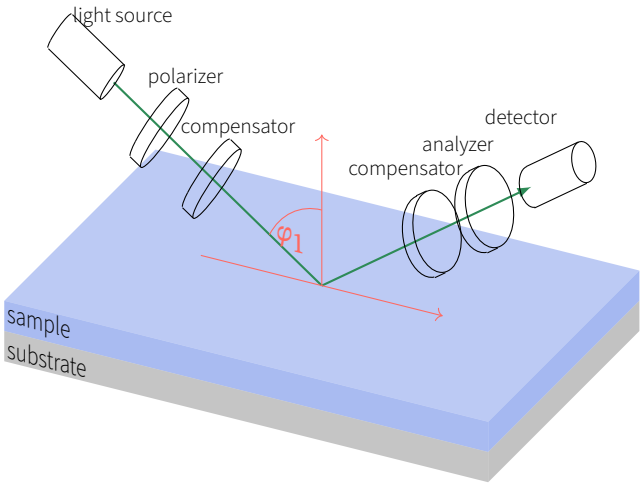

Fig. 4 | Schematic setup of an ellipsometry experiment.

– often a quarter-wave plate – introduces a phase difference between the p- and s-polarized components, establishing a known state for the electric (E) vector of the light. The light then impinges on the sample surface, where it undergoes partial reflection and transmission. The transmitted light is reflected at each interface (such as those between air, the sample, and the substrate), resulting in a superposition of all light rays exiting the sample. This composite light then passes through the second compensator and a subsequent anlalyzer (a second polarizer) to determine its polarization state before reaching the detector. At the detector, changes in the polarization state of the light are quantified. The primary measured parameters are the ellipsometric angles, Ψ (Psi) and Δ (Delta). For our analysis we express the E-vector of the incident and reflected light respectively in the form of so called Jones vectors:

$$\boldsymbol{E}^i = \begin{bmatrix} E^i_\parallel \\ E^i_\perp \end{bmatrix} = \begin{bmatrix} A^i_\parallel \exp\{i\delta^i_\parallel\} \\ A^i_\perp \exp\{i\delta^i_\perp\} \end{bmatrix} \tag{6}$$

$$\boldsymbol{E}^r = \begin{bmatrix} E^r_\parallel \\ E^r_\perp \end{bmatrix} = \begin{bmatrix} A^r_\parallel \exp\{i\delta^i_\parallel\} \\ A^r_\perp \exp\{i\delta^i_\perp\} \end{bmatrix} \tag{7}$$

Using (6) and (7) Ψ is thus defined by:

$$\tan(\Psi) = \left(\left| \frac{A^r_\parallel / A^i_\parallel}{A^r_\perp / A^i_\perp} \right| \right) \tag{8}$$

And Δ will be defined as:

$$\Delta = \left(\delta^r_\parallel - \delta^r_\perp\right) - \left(\delta^i_\parallel - \delta^i_\perp\right) \tag{9}$$

By inserting Fresnel equations (4) and (2), we arrive at the fundamental ellipsometric equation:

$$\tan(\Psi)\exp\{i\Delta\} = \frac{r_p}{r_s} \tag{10}$$

Let us explore how this equation can be employed to determine the thickness and refractive index using ellipsometric measurements. We will focus on the simplest scenario: a single thin film layer with a real-valued refractive index n_1 positioned on a substrate with a real-valued refractive index n_2. Figure 5 illustrates the schematic representation of this system. As shown, the expressions for the reflection coefficients r_p and r_s are derived by summing the amplitudes of all light paths exiting the surface. The individual values of these amplitudes are calculated by multiplying the appropriate Fresnel coefficients. It is easy to see that this

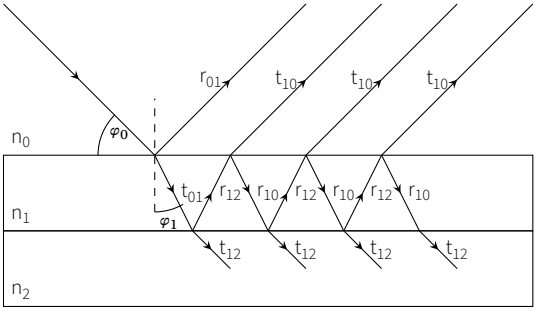

Fig. 5 | Optical model for an ambient/film/substrate system.

process leads to geometric series expressions for the reflection coefficients of p- and s-polarized light, which can be expressed solely using the reflection coefficients, following the relationships $r_{nm} = -r_{nm}$ and $t_{nm}t_{mn} = 1 - r_{nm}^2$. The complete derivation is detailed in [18] and will not be reproduced here since it is rather lengthy. The coefficients are expressed as:

$$r_{012,p} = \frac{r_{01,p} + r_{12,p}\exp\{-i2\beta\}}{1 + r_{01,p}r_{12,p}\exp\{-i2\beta\}} \tag{11}$$

$$r_{012,s} = \frac{r_{01,s} + r_{12,s}\exp\{-i2\beta\}}{1 + r_{01,s}r_{12,s}\exp\{-i2\beta\}} \tag{12}$$

Here β represents the so called phase thickness which is related to the film thickness d and its refractive index n_1 by:

$$\beta = 2\pi d n_1 \cos(\varphi_1/\lambda) \tag{13}$$

Using (11) and (12), the fundamental ellipsometric equation can be expanded:

$$\tan(\Psi)\exp\{i\Delta\} = \frac{\frac{r_{01,p}+r_{12,p}\exp\{-i2\beta\}}{1+r_{01,p}r_{12,p}\exp\{-i2\beta\}}}{\frac{r_{01,s}+r_{12,s}\exp\{-i2\beta\}}{1+r_{01,s}r_{12,s}\exp\{-i2\beta\}}} \tag{14}$$

By examining (11), (12) and (13), we find that due to the periodicity of the complex exponential our solutions will be ambiguous. This phenomenon known as thickness ambiguity arises as light travels through the film, accumulating phase shifts that contribute to the interference pattern, which is periodic in nature. Hence, for a given set of ellipsometric angles (Ψ and Δ), several combinations of film thickness and refractive index can satisfy the same measured values due to this periodicity. Without additional information or constraints, it becomes difficult to uniquely determine the exact physical thickness of the film. To resolve this ambiguity, spectroscopic ellipsometry is often employed, which involves measuring Ψ and Δ across a range of wavelengths. Usually, a fitting procedure is employed in which additional data points help differentiate between the possible solutions, reducing ambiguity. Moreover, the use of accurate models and additional constraints, such as known material properties or pre-measured film parameters, can help refine thickness calculations and alleviate the ambiguity. Choosing the appropriate model is the most crucial and intricate part of the fitting process when deriving optical parameters. Two principal methods can be utilized for modeling and fitting analysis: the widely used parameterized or oscillator model, and the wavelength-by-wavelength best-match model [19, 18].

REFERENCES

[1] E. Hecht. *Optics*. Pearson Education, Incorporated, 2017. ISBN: 978013397722 URL: https://books.google.de/books?id=ZarLoQEACAAJ.

[2] Govind P. Agrawal. "Chapter 5 - Fiber lasers". In: *Applications of Nonlinear Fiber Optics (Third Edition)*. Ed. by Govind P. Agrawal. Third Edition. Academic Press, 2021, pp. 193–254. ISBN: 978-0-12-817040-3. DOI: https://doi.org/10.1016/B978-0-12-817040-3.00011-0. URL: https://www.sciencedirect.com/science/article/pii/B9780128170403000110.

[3] Denis Vincent and John W. Y. Lit. "Thin-film beam splitter for integrated optics". In: *J. Opt. Soc. Am.* 67.4 (Apr. 1977), pp. 533–538. DOI: 10.1364/JOSA.67.000533. URL: https://opg.optica.org/abstract.cfm?URI=josa-67-4-533.

[4] Omega Optical. *Hot vs Cold Mirror*. June 2021. URL: https://omega-optical.com/blog/hot-mirror-vs-cold-mirror/ (visited on 11/21/2024).

[5] Yusuf Dogan, İlhan Erdogan, and Ali Altuntepe. "Design and fabrication of highly efficient antireflective coating in MWIR on germanium using ion-assisted e-beam deposition". In: *Optical Materials* 157 (2024), p. 116362. ISSN: 0925-3467. DOI: https://doi.org/10.1016/j.optmat.2024.116362. URL: https://www.sciencedirect.com/science/article/pii/S0925346724015453.

[6] Adem Yenisoy et al. "Ultra-broad band antireflection coating at mid wave infrared for high efficient germanium optics". In: *Opt. Mater. Express* 9.7 (July 2019), pp. 3123–3131. DOI: 10.1364/OME.9.003123. URL: https://opg.optica.org/ome/abstract.cfm?URI=ome-9-7-3123.

[7] Ashish Varade et al. "Diamond-like Carbon Coating Made by RF Plasma Enhanced Chemical Vapour Deposition for Protective Antireflective Coatings on Germanium". In: *Procedia Materials Science* 5 (2014). International Conference on Advances in Manufacturing and Materials Engineering, ICAMME 2014, pp. 1015–1019. ISSN: 2211-8128. DOI: https://doi.org/10.1016/j.mspro.2014.07.390. URL: https://www.sciencedirect.com/science/article/pii/S221181281400755X.

[8] Ömer Kesmez et al. "Preparation and characterization of multilayer anti-reflective coatings via sol-gel process". In: *Ceramics International* 44.3 (2018), pp. 3183–3188. ISSN: 0272-8842. DOI: https://doi.org/10.1016/j.ceramint.2017.11.088. URL: https://www.sciencedirect.com/science/article/pii/S0272884217325439.

[9] Deepika Gupta et al. "High energy (MeV) ion beam induced modifications in Al2O3-ZnO multilayers thin films grown by ALD and enhancement in photoluminescence, optical and structural properties". In: *Vacuum* 192 (2021), p. 110435. ISSN: 0042-207X. DOI: https://doi.org/10.1016/j.vacuum.2021.110435. URL: https://www.sciencedirect.com/science/article/pii/S0042207X21003869.

[10] Vivechana Agarwal and Jesus Del Río. "Tailoring the photonic band gap of a porous silicon dielectric mirror". In: *Applied Physics Letters* 82 (Mar. 2003), pp. 1512–1514. DOI: 10.1063/1.1559420.

[11] D. Moctezuma-Enriquez R. Archuleta-Garcia and J. Manzanares-Martinez. "Enlargement of Photonic Band Gap in Porous Silicon Dielectric Mirrors". In: *Journal of Electromagnetic Waves and Applications* 24.2-3 (2010), pp. 351–361. DOI: 10.1163/156939310790735732. URL: https://doi.org/10.1163/156939310790735732.

[12] R. Waser. *Nanoelectronics and Information Technology: Advanced Electronic Materials and Novel Devices*. Wiley, 2012. ISBN: 9783527409273. URL: https://books.google.de/books?id=1PgYS7zDCM8C.

[13] Harald Ibach and Hans Lüth. "Motion of Electrons and Transport Phenomena". In: *Solid-State Physics: An Introduction to Principles of Materials Science*. Berlin, Heidelberg: Springer Berlin Heidelberg, 2009, pp. 241–290.

[14] "Electrochemical Pore Formation". In: *Electrochemistry of Silicon*. John Wiley & Sons, Ltd, 2002. Chap. 6, pp. 97–126. ISBN: 9783527600274. DOI: https://doi.org/10.1002/3527600272.ch6. eprint: https://onlinelibrary.wiley.com/doi/pdf/10.1002/

3527600272.ch6. URL: https://onlinelibrary.wiley.com/doi/abs/10.1002/3527600272.ch6.

[15] V Lehmann. "Porous silicon formation: A quantum wire effect". In: *Applied Physics Letters* 58.8 (1991), pp. 856–858.

[16] Hans Artmann. "Poröses Silizium als neuartiges Material in der Mikrosystemtechnik". PhD thesis. Fritschestr. 68, 10 585 Berlin: University of Stuttgart, June 2001.

[17] W. Theiß. "Optical properties of porous silicon". In: *Surface Science Reports* 29.3 (1997), pp. 91–192. ISSN: 0167-5729. DOI: https://doi.org/10.1016/S0167-5729(96)00012-X. URL: https://www.sciencedirect.com/science/article/pii/S016757299600012X.

[18] Tobias Holmgaard Jesper Jung Jakob Bork and Niels Anker Kortbe. *Ellipsometry*. Pontoppidanstræde 103 - 9220 Aalborg Øst, Dec. 2004. URL: https://homes.nano.aau.dk/kp/Ellipsometry/main.pdf.

[19] "Principles of Spectroscopic Ellipsometry". In: *Spectroscopic Ellipsometry*. John Wiley & Sons, Ltd, 2007. Chap. 4, pp. 81–146. ISBN: 9780470060193. DOI: https://doi.org/10.1002/9780470060193.ch4. eprint: https://onlinelibrary.wiley.com/doi/pdf/10.1002/9780470060193.ch4. URL: https://onlinelibrary.wiley.com/doi/abs/10.1002/9780470060193.ch4.